Molecular Catalysis 528 (2022) 112475

Contents lists available at ScienceDirect

Molecular Catalysis

journal homepage: www.journals.elsevier.com/molecular-catalysis

The effects of facet-dependent palladium-titania interactions on the activity of Pd/Rutile catalysts for lean methane oxidation

Cunshuo Li [a,b], Bingyue Tang [a,b], Ajibola T. Ogunbiyi [a,b], Songquan Tang [a,b], Wenzhi Li [a,b,*], Qiang Lu [b,c], Liang Yuan [b,d]

[a] Department of Thermal Science and Energy Engineering, University of Science and Technology of China, Hefei 230026, China
[b] Institute of Energy, Hefei Comprehensive National Science Center, Hefei 230031, China
[c] National Engineering Laboratory for Biomass Power Generation Equipment, North China Electric Power University, Beijing 102206, China
[d] National and Local Joint Engineering Research Center of Precision Coal Mining, Anhui University of Science and Technology, Huainan 232001, China

ARTICLE INFO

Keywords:
Pd/Rutile catalysts
Facet-dependent effects
Lean methane oxidation

ABSTRACT

Rod-shaped rutile materials with different proportions of (110) and (111) facets exposed were hydrothermally prepared, and the facet-dependent effects of rutile on the activity of supported palladium phases in lean methane oxidation were elucidated. Although a stronger interaction between palladium and the rutile (111) facet was confirmed by systematic characterizations, performance evaluation and *in situ* DRIFTS revealed deteriorated catalytic efficiencies of palladium catalysts. Specifically, while complete methane oxidation was achieved at temperature below 450 °C over a Pd/Rutile-(110) catalyst, only 39% of methane were eliminated at 500 °C over its counterpart supported on Rutile-(111). Investigations on rutile supported palladium catalysts further revealed that the facet-dependent palladium-titania interactions profoundly affected the particle sizes and chemical states of the deposited palladium species. In combination with DFT calculations, it was then found that Pd^{4+} species that might function synergistically with Pd^{2+} in methane activation were not as stable on the rutile (111) facet, due to the strong electron transfer from this substrate. It is hoped that the conclusions drawn in this work would provide supplementary understanding of the facet-dependent metal-TiO_2 interactions and some inspirations on the further rutile-related catalyst design.

1. Introduction

Catalytic oxidation represents an economical and effective elimination route for methane, which is the second largest contributor to greenhouse effect [1–4]. The main technical difficulty of this route lies in the development of catalyst materials, because methane, the most refractory hydrocarbon, cannot be catalytically oxidized readily at low temperatures. After decades of research, palladium based catalysts have been screened as the benchmark candidates for the catalytic combustion of methane (CCM) [5–12]. There is a general consensus that the catalytic efficiencies of palladium in CCM reaction strictly correlate with its particle size [13,14], chemical state [15,16], morphology [17,18], etc. All the stated properties, on the other hand, can be manipulated by interactions between palladium and its host materials. Many palladium catalysts deposited on metal oxides, in which strong metal-support interactions (SMSI) were established via intensive electron transfers, were thus reported by researchers to further reveal their structure-activity relationships [19–24].

Titanium oxide (TiO_2) is widely involved in catalytic oxidation reactions, especially as a catalyst carrier, because of its reducible nature that contributes to the regeneration of active phases. Extensive studies have reported the application of TiO_2-supported catalysts in the catalytic oxidation of carbon monoxide [25,26], hydrocarbons [27,28], soot [29,30], etc. For CCM reaction, we believe that the rutile phase of titania is more competitive than anatase for at least two reasons. First, the SMSI-induced decoration (encapsulation) of supported entities by anatase phase, which generally occurred at high temperatures, covers active sites and thus becomes detrimental to the efficient oxidation of methane. Although Tang et al. [31] have illustrated the anti-encapsulation property of anatase (001) facet under CCM reaction conditions, the preparation of anatase nanosheet that exposes the (001) plane required complex and stepwise hydrothermal processes, not to mention its extremely low yield. At the same time, other researchers found that the decoration effect arising from the reductive atmosphere

* Corresponding author at: Department of Thermal Science and Energy Engineering, University of Science and Technology of China, Hefei 230026, China.
E-mail address: liwenzhi@ustc.edu.cn (W. Li).

https://doi.org/10.1016/j.mcat.2022.112475
Received 18 May 2022; Received in revised form 21 June 2022; Accepted 23 June 2022
Available online 28 June 2022

got more mitigated in rutile supported catalysts than that in its anatase supported counterparts [32,33]. Although the mechanisms of encapsulation induced by high temperatures and reductive treatments may be different, a better property of rutile phase was still reasonably expected. Secondly, TiO_2 anatase is thermodynamically less stable than TiO_2 rutile, as the former phase will transform into rutile at temperatures higher than 600 °C [34]. Still worse, such a transformation might occur at lower temperatures under the implication of its supported phases like PdO [35] and CuO [36]. The reconstruction of its supported species, in this case, would be inevitable and finally result in their annihilation. Therefore, rutile materials possessing the superiorities of titania but without the shortcomings of anatase phase are expected to be excellent carriers for CCM catalysts.

Facet-dependent metal-support interactions in numerous catalyst systems based on reducible oxides like CeO_2 [37,38], Co_3O_4 [39,40], TiO_2 (anatase phase) [29,41] have been studied and proven to have profound effects on the completion of oxidation reaction. To our knowledge, however, research on the facet engineering of rutile materials and corresponding structure-activity relationships in CCM reaction were rarely reported. Enlightened by related advances in material science [42–44], we recently succeeded in the synthesis of rutile materials that possess rod-like morphology with different aspect ratios. As illustrated in Scheme 1, the rod-shaped rutile material, which is produced via the hydrolysis of titanium precursor using glycolic acid as template, consists of four lateral sides and two tapered tops that expose (110) and (111) facets, respectively. Based on this material, the growth of low-energy (110) surface could be hampered under the modification of F-, and thus, these nanorods would be truncated and more (111) facet exposed [42]. Likewise, via adjusting the type of titanium precursor and hydrothermal parameters, rutile nanorods possessing larger aspect ratio, i.e., higher proportion of (110) facet, could also be synthesized [43,44]. In short, these works enabled us to prepared well-defined rutile materials that preferentially expose the (110) and (111) facets and actually make the investigations on the properties of these two facets possible.

Herein, palladium nanoparticles were deposited on three rod-shaped rutile materials with decreasing aspect ratios to understand the interplay between palladium and two rutile facets for CH_4 oxidation. The successful synthesis of specific rutile materials that preferentially expose the (110) and (111) facets and their diverse physiochemical properties were first confirmed via systematic characterizations. The catalytic activities of palladium catalysts supported on these rutile materials were also examined. Combined subsequent investigations with DFT calculations, the effects of the electronic interactions between rutile and palladium, which largely determined the particle sizes of palladium and the stability of Pd^{4+} species, were finally elucidated to reveal the structure-activity relationships in a Pd/Rutile catalyst system.

2. Experimental section

2.1. Preparation of truncated rod-like rutile exposing (111) facet

In this manuscript, the rod-like rutile material illustrated in Scheme 1 were denoted as Rutile-mixed since it exposed both the (110) and (111) facets. For its preparation, 5.0 mL titanium butoxide was first added dropwise to 150 mL solution of glycolic acid (1.0 M) to form a bluish suspension and then heated at 90 °C for 2 h to get a water miscible solution. Subsequently, the resulting solution and a 7.5 mL NaF solution (0.6 M) were mixed in Teflon-lined autoclaves and maintained at 200 °C for 24 h. The rutile was then centrifuged and washed repeatedly with ethanol and distilled water, and the as-dried sample was calcined at 600 °C for 4 h to obtain the final product. The preparation of the rutile material exposing more fractions of the (111) facet, designated as Rutile-(111), was the same as that of Rutile-mixed except that the dosage of NaF was doubled. It is worthy of note that Rutile-mixed and Rutile-(111) were sufficiently washed and annealed at high temperatures to remove fluorine-containing and organic substances.

2.2. Preparation of rod-like rutile mainly exposing the (110) facet

Similar to that of Rutile-mixed and Rutile-(111), the synthesis of rod-like rutile with larger aspect ratio also necessitated the use of glycolic acid as a template, but the titanium precursor was altered to titanium tetraisopropoxide. Typically, 10.0 mL titanium tetraisopropoxide and 10.0 mL isopropanol were added into a 100 mL solution of glycolic acid (1.6 M) to form a white suspension and then heated to 90 °C for 2 h to give a transparent solution. The resulting solution was then sealed in Teflon-lined autoclaves and held at 200 °C for 24 h. The rutile powders were separated by centrifugation and washed with ethanol before drying at room temperature. The titania mainly exposing the (110) facet was finally annealed at 600 °C for 4 h and the material obtained was denoted as Rutile-(110).

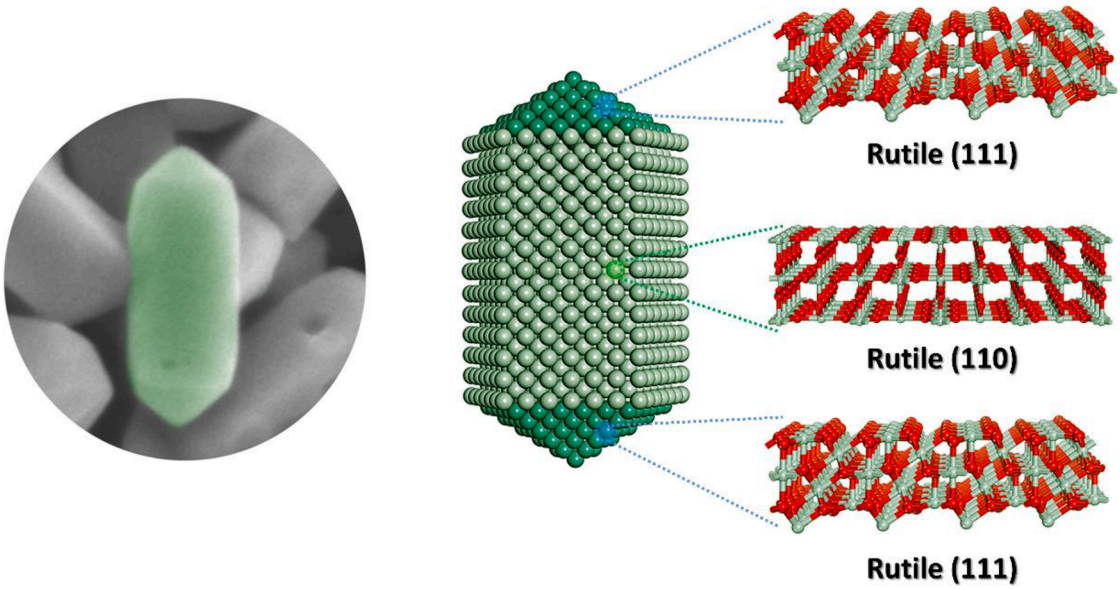

Scheme 1. The schematic illustration of rod-like rutile material exposing (110) and (111) facets in corresponding regions.

2.3. The deposition of palladium on rutile materials

0.5 g rutile materials were added to a 25.1 mL solution of palladium nitrate precursor (1.0 mg/mL) and then stirred overnight. To ensure that the loadings of palladium were the same on three samples, the suspensions were stirred at 90 °C until all the solvent evaporated. The obtained samples containing 2.0 wt% palladium were calcined at 500 °C for 4 h to obtain the Pd/Rutile catalysts.

2.4. Computational methods

The DFT calculations in this work were performed using Cambridge Sequential Total Energy Package (CASTEP). The generalized gradient approximation (GGA) of Perdew-Burke-Ernzerhof (PBE) exchange-correlation functional was applied for geometric optimization. A cut-off energy of 500 eV was employed to ensure the accuracy of structural optimization, and the atomic structures were relaxed until the maximum force upon each unconstraint atom was less than 0.05 eV $Å^{-1}$. The Brillouin-zone integration of rutile (110) and rutile (111) systems were performed along with 3 × 3 × 1 Monkhorst-Pack grids. The vacuum separation between each slab was 15 Å in both systems to avoid the interactions between the neighboring slabs. The binding energy (E_{bind}) of the palladium entities on rutile surface were used to reflect their interaction strength with different rutile facets here, and the expression of E_{bind} is

$$E_{bind} = E(PdO_x / rutile) - -E(rutile) - -E(PdO_x) \quad (1)$$

where E (PdO_x/rutile), E (rutile), and E (PdO_x) are the total energies of the rutile substrates with PdO_x entities, the rutile substrates, and PdO_x entities.

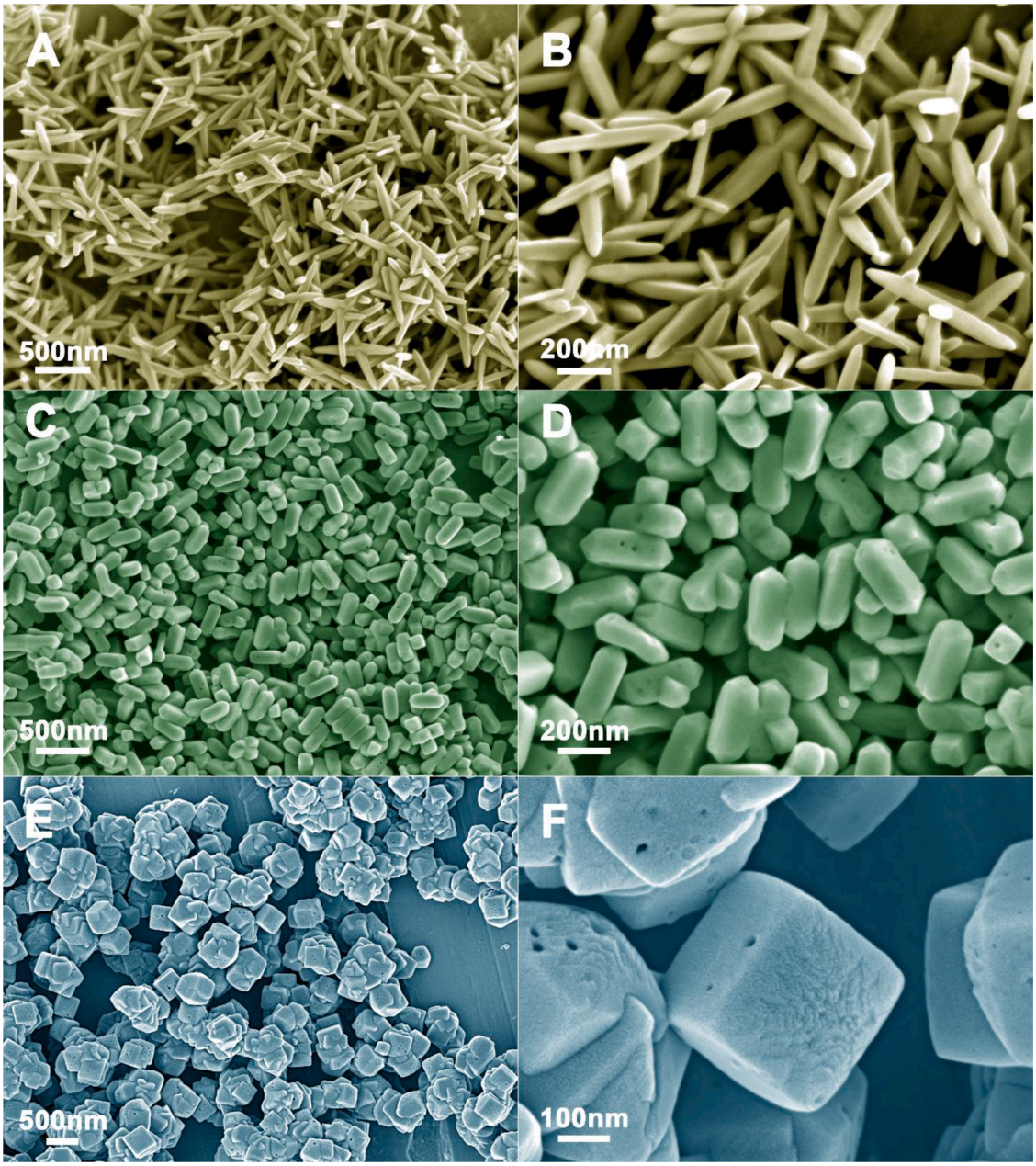

Fig. 1. The SEM images of (A, B) Rutile-(1 1 0), (C, D) Rutile-mixed, and (E, F) Rutile-(1 1 1) at high and low magnifications, respectively.

3. Results and discussion

3.1. The microscopic and texture properties of rutile materials

To investigate the actual microstructures of our rutile materials, their SEM images were first taken and displayed in Fig. 1. Together with the schematic illustration in Scheme 1, the successful preparation of Rutile-mixed material was confirmed. The SEM images shown in Fig. 1C and D revealed its rod-like morphology with an average length of about 400 nm, and its aspect ratio was estimated to be approximately 4.0. Although the lateral sides of both Rutile-(110) and Rutile-mixed exposed the (110) planes theoretically, the former material whose SEM images were shown in Fig. 1A and B was definitely more suitable for studying the roles of the (110) plane, thanks to its larger aspect ratio (near 10.0). As introduced, under the modification of F^-, the middle part of Rutile-mixed could be further truncated and thus the ratio of the (111) plane exposed on the tapered tops was significantly increased in Rutile-(111) sample, see Fig. 1E and F. To verify our assignments, the lateral sides of Rutile-(110) and Rutile-mixed along with the tapered top of Rutile-(111) (marked with circles in Fig. 2A, C and E) were inspected by the TEM technique. Based on the results of their HRTEM images, we measured the corresponding lattice fringes (shown in Fig. 2B, D and F) to be ~ 0.33 and 0.22 nm, respectively, demonstrating that the rod-shaped rutile materials did expose the (110) and (111) facets in selected regions [42, 45,46]. In brief, the microscopic techniques used here visualized the well-defined rutile materials preferentially exposing the (110) and (111) facets and thus ensured the reliability of a follow-up research. The additional research on Rutile-mixed material, on the other hand, would provide supplementary evidences of the roles played by two facets.

The N_2-sorption experiments of three samples were then carried out to study their textural properties. As can be seen from Fig. 3A, the isotherms of both Rutile-(110) and Rutile-mixed showed rapid increases in the quantity of N_2 adsorbed at high relative pressures (> 0.95), which signified the presence of mesopores with relatively large size. However, the calculated BET surface area of the former sample (20.7 m^3/g) was more than twice the latter (9.7 m^3/g) due to their different adsorption capacities, and their porosity parameters also showed slight differences (Table 1 and Fig. S1). The subsequent deposition of palladium did not remarkably alter the adsorption properties (Fig. S2) and the calculated parameters (Table S1) of these two samples. For Rutile-(111) sample, a H4 type loop, generally caused by mesoporous structures, appeared in its isotherm profile. Based on the observation of its enlarged SEM image in Fig. 1F, we realized that this special pattern might be associated with the cavities presented on the surface of Rutile-(111) material. Although

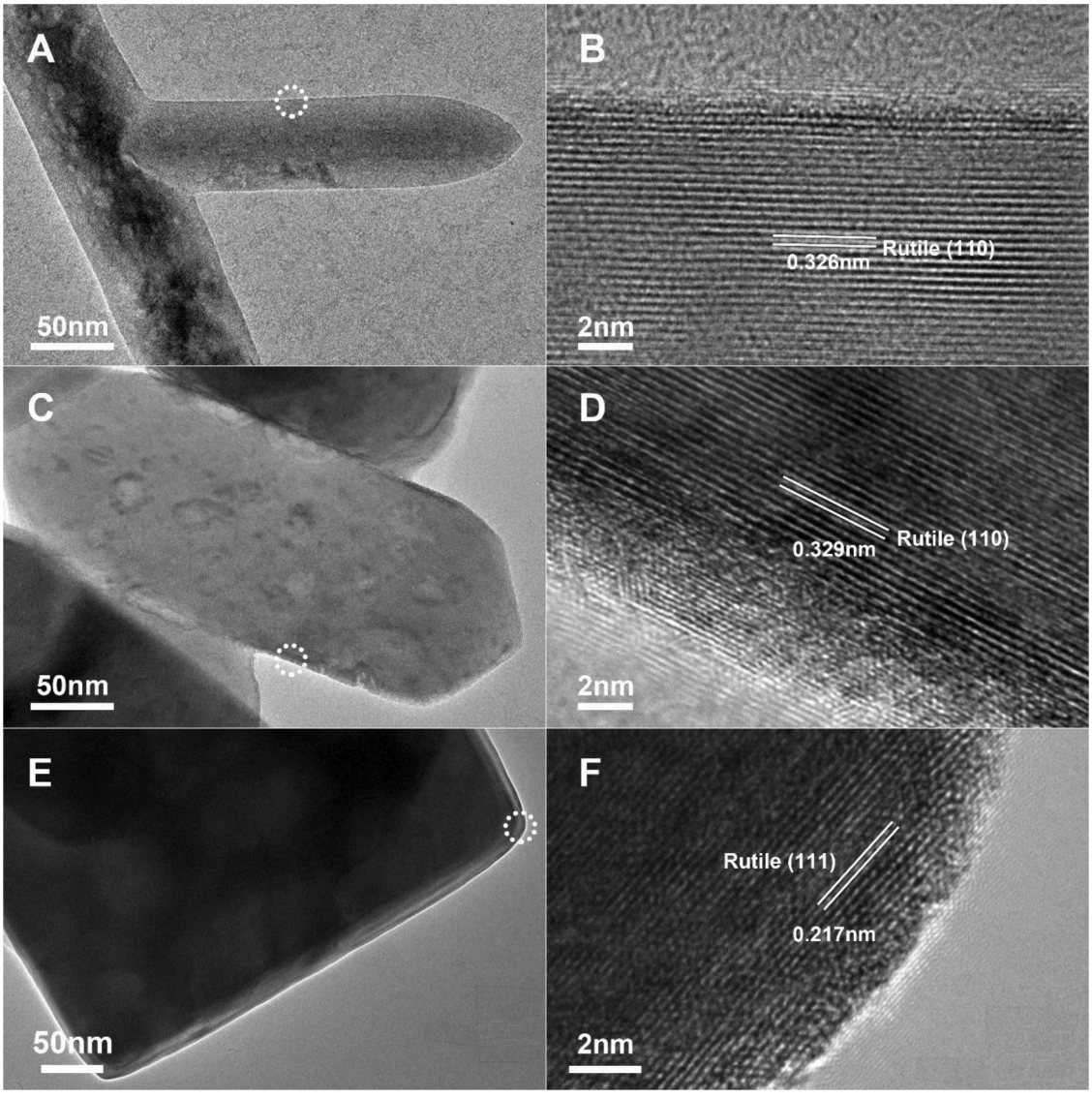

Fig. 2. The TEM and HRTEM images of (A, B) Rutile-(100), (C, D) Rutile-mixed, and (E, F) Rutile-(111) samples.

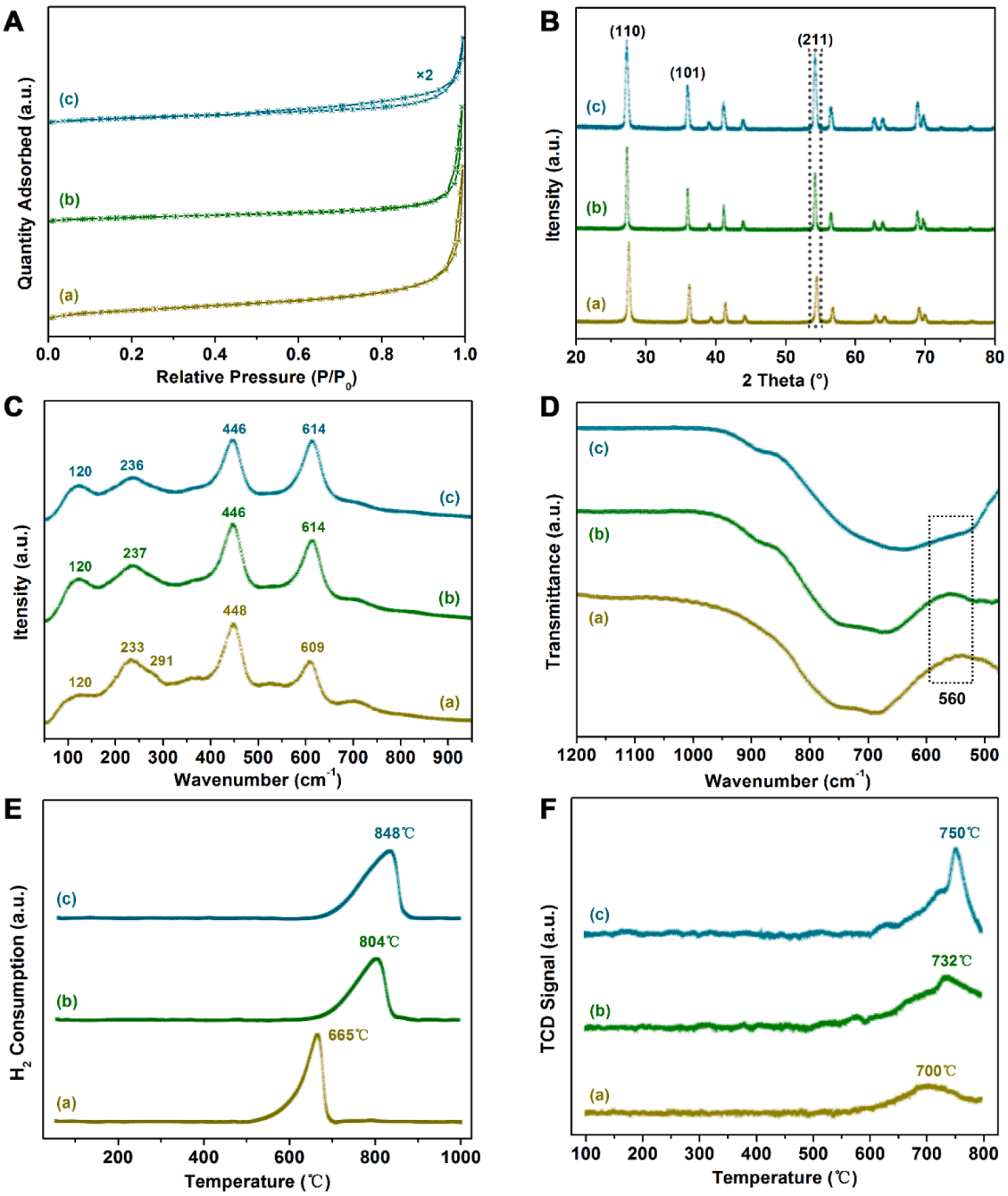

Fig. 3. The (A) N_2-sorption isotherms, (B) XRD patterns, (C) Raman spectra, and (D) FT-IR spectra, (E) H_2-TPR and (F) O_2-TPD profiles of (a) Rutile-(110), (b) Rutile-mixed, and (c) Rutile-(111).

Table 1
The textural and physiochemical properties of rutile materials.

	Surface Area [a] m^3/g	Pore Volume [b] cm^3/g	Pore Size [b] Å	O_2 Desorption [c] μmol/g
Rutile-(1 1 0)	20.7	0.08	16.2	115.4
Rutile-mixed	9.7	0.06	24.0	128.3
Rutile-(1 1 1)	5.3	0.02	16.0	283.2

a, b: Calculated based on BET equation and BJH model, respectively.
c: Obtained from the results of O_2-TPD experiments.

the formation mechanism of these cavities was still under investigation, however, given the relatively small BET surface areas and porosity parameters of this sample (see Table 1), its textural property might not leave large variations on the palladium-rutile interaction.

3.2. *The physiochemical properties of rutile materials*

The XRD patterns (Fig. 3B) that matched the JCPDS #65-0190 of rutile phase well without any other phase detected then confirmed the purity of the three samples. However, detailed inspection illustrated that, while the diffractions related to the (110) and (101) facets were kept almost constant, the intensities of the (211) signals increased gradually in the patterns of Rutile-mixed and Rutile-(111). Since the diffractions of X-ray closely correlate with the crystalline orientations of

detected samples, this trend might result from the different arrangements of surface atoms in the three rutile materials. For better understanding of this observation, we next resorted to Raman and FT-IR techniques that are highly sensitive to the vibration modes of metal-oxygen bonds. In the Raman spectra recorded in Fig. 3C, it was first found that the intensity of rutile A_{1g} mode [36] located at ~ 610 cm^{-1} strengthened with the increased proportions of (111) facet, and this band shifted from 609 cm^{-1} in Rutile-(110) to 614 cm^{-1} in Rutile-mixed and Rutile-(111). In addition, as the Raman bands of Rutile-(111) at wavenumbers below 300 cm^{-1} resembled that of Rutile-mixed, these characteristics varied in the results of Rutile-(110). When the incident light source was turned to infrared ray, the broad FT-IR signals ranged from 500 - 1000 cm^{-1}, which were characteristic of Ti-O vibrations in TiO_6 octahedron [47], also possessed exclusive shapes and positions in their FT-IR scans (Fig. 3D). The vibration modes of Ti-O bonds reflected by spectroscopic techniques indicated that the coordination between titanium with oxygen, which largely determined the number of under-coordinated Ti 5c sites exposed, might have varied with the alternation of their morphologies. Considering that the deposited metal atoms generally bonded with unsaturated titanium sites directly or via bridge oxygen sites [48,49], such a difference would inevitably affect the structural and catalytic properties of their supported phases.

The temperature programmed techniques were then employed for studying the states of Ti-O bonds in the three materials. The results shown in Fig. 3E and F first supported the thermally stable nature of rutile materials, because the signal changes of all the three samples occurred at temperatures higher than 500 °C. This conclusion demonstrated that all the three rutile materials could provide stable chemical environments for the residue of palladium precursors. For their differences, it was first found that the redox ability of Rutile-(110) was visibly superior to those of the other two samples, as its reduction started and maximized earlier. Such an observation was actually in line with the higher Ti 2p binding energy of Rutile-(110) (vide infra), revealing the electron-deficient feature of this sample. On the other hand, as reflected by the O_2-TPD profiles in which the TCD signals of O_2 desorption detected at temperatures above 700 °C were caused by lattice oxygen species [50,51], the decomposition of Rutile-(110) was weaker than its counterparts instead. It must be emphasized that the positive TCD signals in Fig. 3F might not be completely caused by the liberation of oxygen, since the condenzation of surface hydroxyl groups or desorption of other chemisorbed gases could also give TCD signals. Even so, the quantities of lattice oxygen desorbed (see Table 1) from our samples were almost negligible when compared with their theoretical oxygen content (12.5 mmol/g), further verifying the high stability of our rutile materials.

3.3. The facet-dependent rutile-palladium interactions

To study the facet effect of rutile on the palladium-support interactions, 2.0 wt% palladium (determined by ICP-AES, see Table 2) was deposited on the three rutile materials via an impregnation method. The dispersion states of palladium species were first investigated by their TEM and STEM images, in which palladium particles appeared as black and bright spots, respectively. With the complementary contrasts of the TEM and STEM techniques, we then plotted the size distribution histograms of palladium particles (the insets of Fig. 4A–C) and calculated the average sizes of palladium particles on the three rutile materials to be 7.8, 7.4 and 5.4 nm in sequence. Such statistics were consistent with the STEM-EDS elemental mappings of Fig. 4D–F shown in Fig. S3. While the bright regions with slight aggregation in Fig. 4D and E were visualized by Pd Lα1 signals in Fig. S3A and B, uniform inclusion of palladium in Pd/Rutile-(111) were confirmed in Fig. S3C. Correspondingly, the XRD patterns of these three samples (Fig. S4) also presented gradually weakened palladium diffractions at ~34° with the exposure of the rutile (111) facet. Meanwhile, the atomic ratios of palladium to titanium detected by XPS (Table 2) also increased from 0.142 in Pd/Rutile-(110) to 0.167 in Pd/Rutile-mixed and finally 0.268 in Pd/Rutile-(111), which was in line with their decreasing particle sizes. Therefore, these observations exemplified that the particle sizes of palladium species were under the influence of the diverse titania-palladium interactions in our Pd/Rutile system.

To provide electronic insights on the titania-palladium interactions, we then compared the Ti 2p and O 1 s XPS spectra of three rutile materials with those of their supported palladium catalysts. Consistent with their different physiochemical properties, in Fig. 4G–I, we first noticed that the binding energies (B.E.) of Ti 2p in bare rutile materials decreased from 458.46 to 458.40 and then 458.32 eV with the increasing exposure of the (111) facet. After the deposition of palladium phase, the values of all the three systems shifted to higher energies, indicative of the electron donations of the titanium element. Interestingly, this offset in Rutile-(111) system (0.32 eV) was larger than those in Rutile-mixed (0.17 eV) and Rutile-(110) (0.10 eV) samples. As the driving force of electron transfer originates from the difference in the work function between electron-donator and receptor [52], different degrees of XPS offsets actually accounted for the varied electronic structures of the rutile (110) and (111) facets. Analogous evidence was then obtained from the O 1 s XPS spectra shown in Fig. 4J–K, in which the offset trends of oxygen element were similar to that of titanium. Based on the results gathered, it was tentatively concluded that the electrons of both oxygen and titanium might have been donated to the palladium phases in our catalyst system. And conceivably, stronger palladium-rutile interactions would be established with the increased proportions of exposed the rutile (111) facet. According to the works that we and other researchers have done, we propose that the intensive metal-support interaction in Pd/Rutile-(111) catalyst might have two fold impacts on its catalytic performance. On the positive side, such an interaction would definitely contribute to the dispersion of palladium phase and make more active sites accessible, finally endowing this sample with desired catalytic properties. On the other hand, too strong palladium-titania interaction might also induce the encapsulation of palladium by titania, just as reported in the anatase supported palladium catalyst system [31], resulting in the performance deterioration of the catalyst materials.

3.4. The catalytic performance of Pd/Rutile catalysts

To verify the actual effect of palladium-rutile interaction on the catalyst performance, the catalytic activities of three palladium catalysts

Table 2
The surface composition and catalytic performance of rutile supported palladium catalysts.

	Pd loading [a] wt%	T_{50} [°C]	T_{90} [°C]	Reaction rate [b] [$\mu mmol_{CH4} g_{Pd}^{-1} s^{-1}$]	Activation energy [KJ/mol]	Pd/Ti [c]	$Pd^{4+}/(Pd^{4+}+Pd^{2+})$ [d] [%]
Pd/Rutile-(110)	1.96	345	397	13.5	103.1	0.142	32.1
Pd/Rutile-mixed	2.05	398	n.a.	2.3	127.7	0.167	22.1
Pd/Rutile-(111)	1.98	483	n.a.	0.2	143.5	0.268	21.9

a: Determined by ICP-AES.
b: Based on the methane conversion measured at 275 °C.
c, d: Obtained from the results of XPS.
n.a.: Not available.

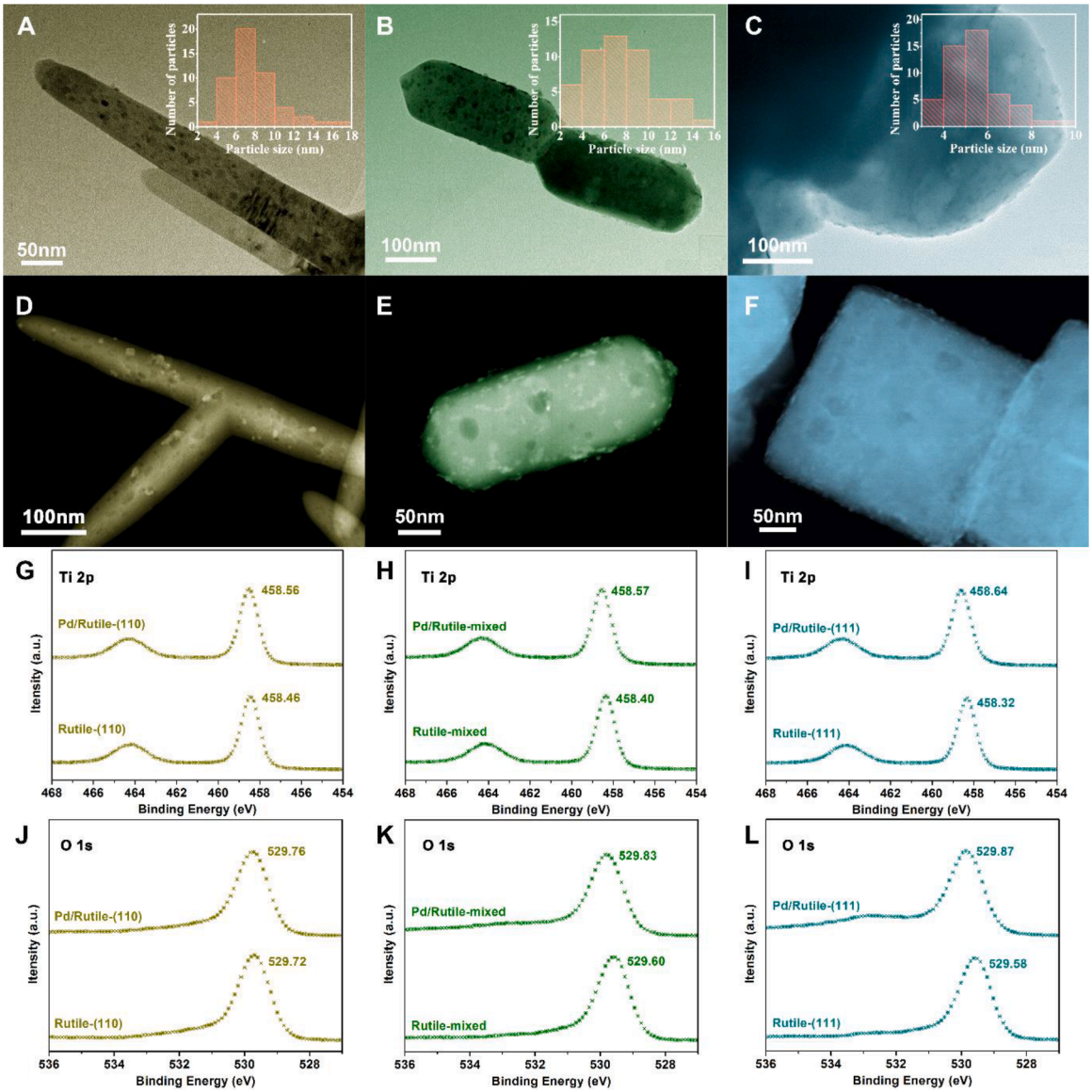

Fig. 4. The TEM images of (A) Pd/Rutile-(110), (B) Pd/Rutile-mixed, and (C) Pd/Rutile-(111). The STEM images of the (D) Pd/Rutile-(110), (E) Pd/Rutile-mixed, and (F) Pd/Rutile-(111). The (G–I) Ti 2p and (J–L) O 1 s XPS spectra of corresponding palladium catalysts along with their support materials.

were examined and their light-off curves were plotted as shown in Fig. 5A. The Pd/Rutile-(100) catalyst, over which the complete conversion of methane was achieved at temperatures below 450 °C, first exhibited a decent activity towards the CCM reaction. The temperature at which the methane conversion over this catalyst reached 50% and 90% were 345 °C and 397 °C, respectively. However, the samples supported on Rutile-mixed and Rutile-(111) materials performed much worse, as the methane conversion over two samples were only 85.4% and 68.7% at 500 °C. The kinetic parameters including the reaction rate at 275 °C (r) and the apparent activation energy (E_a) were also calculated to intuitively reflect the intrinsic catalytic activity of catalyst materials, see Table 2 and Fig. S5. The obtained results revealed the best performance of Pd/Rutile-(110) among the three samples, since the value of its reaction rate (13.5 $\mu mmol_{CH4} g_{Pd}^{-1} s^{-1}$) and activation energy (103.1 KJ/mol) was the highest and the lowest, respectively.

The *in situ* DRIFT spectra of Pd/Rutile-(110) and Pd/Rutile-(111) at reaction atmosphere (350 °C) were also recorded, with corresponding time-dependent spectra plotted in Fig. 5B and C. In accordance with their light-off curves, the infrared signals of product CO_2 (at 2325 cm^{-1}) had comparable intensity to those of CH_4 reactant (at 3014 and 1304 cm^{-1}) in the spectra of Pd/Rutile-(110), but the corresponding CO_2 peaks in Pd/Rutile-(111) sample, although kept strengthening as the time prolonged, were visibly weaker in comparison to those of CH_4. More importantly, the signals of carbonyl (1861 cm^{-1}), H_2O (1615 cm^{-1}) and alcohol (1270 cm^{-1}) species [39,53] did not disappear in the spectrum of Pd/Rutile-(111) even after 30 min, inferring that these intermediates could not decompose or desorb efficiently 350 °C. In contrast, although the signals of formic acid species (at 1560 cm^{-1} [54]) appeared in the spectra of Pd/Rutile-(110) in the first 15 min, no accumulation of any intermediate product occurred over this sample. Therefore, although the strong palladium-support interaction in Pd/Rutile-(111) catalyst effectively dispersed the palladium phases, the SMSI-induced decoration would be its dominant effect. Actually, our recent work has proven that the SMSI-induced encapsulation would take place more readily on the rutile (111) plane than on the rutile (110) plane, and the decoration overlayer would be much more obvious once the work function of the Rutile-(111) material was further lowered (realized by pre-reducing this material under H_2 atmosphere). For providing a comprehensive evaluation, the thermal stability (Fig. S6), water-resistance (Fig. S7A), and hydrothermal stability (Fig. S7B) of the

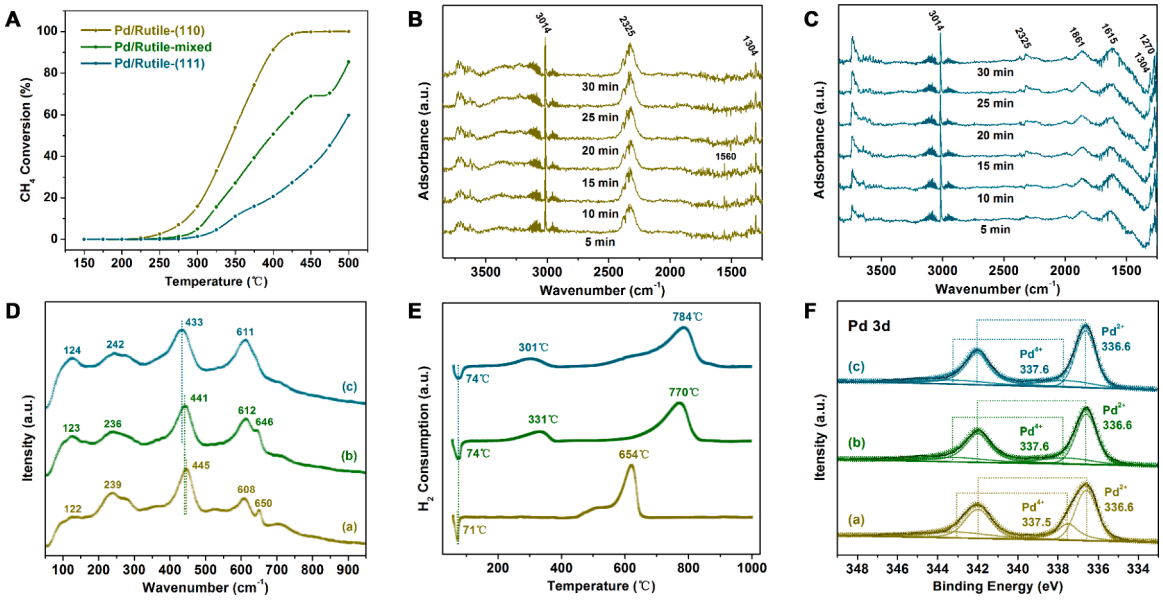

Fig. 5. (A) The light-off curves of supported palladium catalysts. The time-dependent *in situ* DRIFT spectra of (B) Pd/Rutile-(110) and (C) Pd/Rutile-(111) at reaction atmosphere recorded at 350 °C.The (D) Raman spectra, (E) H_2-TPR profiles, and (F) Pd 3d XPS spectra of (a) Pd/Rutile-(110), (b) Pd/Rutile-mixed, and (c) Pd/Rutile-(111).

optimal Pd/Rutile-(110) catalyst were also tested. At dry conditions, our catalyst showed excellent stability at 500 °C, as the methane conversion did not decrease within 24 h. However, when 8.0 vol% water vapor was introduced to the reactant atmosphere, the catalytic performance of this sample, especially at the low-temperature range, deteriorated significantly. The complete methane over this sample was not achievable at 500 °C in the presence of water, and the methane conversion only increased to 47.6% when the temperature reached 600 °C. Moreover, with water introduced, the methane conversion kept decreasing (from 47.6 to 16.1%) in the first 12 h when the reaction was operated at 600 °C. Although the activity of this sample was partially reversible with the removal of water (from 16.1 to 37.2%), the deactivation of palladium phase was still somewhat severe. Here we just remained with reporting the observed trend because the main objective of the present work was elucidating the facet-dependent effect on the activity of rutile-supported palladium catalysts, and work to further improve the water-resistance of the Pd/Rutile-(110) catalyst was already underway in our group.

3.5. *Supplementary evidences for the facet-dependent palladium-rutile interactions*

The paradoxical performance data in the present work suggested that our conclusions should be taken with caution. Therefore, the Raman spectra, H_2-TPR profiles, and Pd 3d XPS spectra of the three palladium catalysts were further obtained to provide more details on the facet-dependent palladium-rutile interactions. For the Raman spectrum shown in Fig. 5D, the deposition of the palladium phase presented signals at 650 and 646 cm^{-1} in the spectrum of Pd/Rutile-(110) and Pd/Rutile-mixed, respectively, while the same feature interfered with the intensified A_{1g} mode of Rutile-(111). Although definitive conclusions could not be drawn based on the characteristics of the palladium species, the observed 4 cm^{-1} offset has inferred their different bonding states with the supports. More importantly, as the TiO_2-related bands of the Pd/Rutile-(110) did not change visibly in comparison to that of Rutile-(110), it was noticed that the most intense E_g band of Rutile-mixed and Rutile-(111), which were centered at same wavenumber (446 cm^{-1}) in the spectra of their initial materials, showed slight broadening and shifted backward to 441 and 433 cm^{-1}, respectively. Such an observation indicated that the vibration frequencies of Ti-O bonds decreased with the deposition of palladium, and the different degrees of redshift of Rutile-mixed and Rutile-(111) demonstrated that this change did derive from the interaction between palladium and rutile-(111) facet. In other words, the results of Raman spectra also confirmed the strongest palladium-titania interaction in the Pd/Rutile-(111) system, which corroborated the analysis of XPS.

The H_2-TPR technique providing the fingerprints of metal-support interactions was utilized again. The profiles of the three samples shown in Fig. 5E all presented negative peaks ranging from 50 to 100 °C, which were caused by the decomposition of PdH_x species [55,56]. However, these signals were centered at higher temperature (74 °C) with the exposure of the rutile (111) facet. These decomposition behaviors of palladium hydrides were expected, since the smaller palladium nanoparticles on the rutile (111) surface generally possessed stronger interactions with their supports and thus were less likely to decompose. Moreover, we found that the reduction behaviors of TiO_2 in Pd/Rutile catalysts also differ from those of their host materials (see Fig. 1E) to some extents. Particularly, while the maximum reduction of Rutile-(110) that occurred at 665 °C shifted to 618 °C, a new reduction peaks at ca. 500 °C appeared in its profile. The main reduction of Pd/Rutile-mixed and Pd/Rutile-(111) also appeared at lower temperature when comparing with their support materials, but the palladium-catalyzed reduction of rutile took place earlier (below 400 °C) in this two samples than that in Pd/Rutile-(110). Given that only the metal phases interacting intimately with metal oxides could alter the redox behaviors of their supports at low temperatures, the stronger titania-palladium interaction in Pd/Rutile-(111) over that of Pd/Rutile-(110) could be safely confirmed.

The O_2-TPD experiments of palladium catalysts were also conducted for providing more information on the palladium-rutile interaction, see Fig. S8. As the catalyst materials were calcined for the second time after the impregnation of palladium precursors, the TCD signals of palladium catalysts were not the same as their support materials. After the deposition of palladium, a new peak appeared at 750–800 °C in the profiles of Pd/Rutile-mixed and Pd/Rutile-(111), which account for the decomposition of PdO species according to our previous work [57]. Although such a signal overlapped with the TCD signals caused by Rutile-(110) material, we still found that the decomposition of PdO on Rutile-(111) surface took place in higher temperature than that on Rutile-mixed, indicating that the palladium species did have stronger interaction

with the rutile (111) facet.

3.6. The effects of palladium-rutile interactions on the chemical states of palladium

With the confirmation of the stronger palladium-rutile interaction in Pd/Rutile-(111) sample, we realized that its effect on the chemical states of the palladium phases should be studied as well to rationalize the performance data. Therefore, we deconvoluted the Pd 3d XPS spectra of the three palladium catalysts in Fig. 5F. The palladium species of all the three samples were predominated in an oxidation state of +2, and the Pd^{4+} species that contributed to the XPS signals at higher B.E. appeared as well [57]. Here, we deduce that the palladium (II) precursors might have been oxidized to form the Pd^{4+} species during the calcination process, and a part of them would transform into PdO species once they received electrons from titania. Based on the integral areas of these two phases, it was found that the proportions of Pd^{4+} species decreased in sequence from 32.1% to 22.1% and 21.9% with the exposure of the rutile (111) facet. The depletion of the Pd^{4+} species was identical to the XPS results in Section 3.3, since more electrons of titanium and oxygen were donated from Rutile-mixed and Rutile-(111) with the deposition of palladium. Regretfully, the Pd^{4+} species might function synergistically with PdO in the activation of methane in our Pd/Rutile catalyst system, especially taking into account that the presence of Pd^{4+} species was the key factor minimizing the activation barrier of methane molecules in reducible oxide supported palladium catalysts [57,58]. In combination with the experimental results and related literatures, we finally conclude that a too strong palladium-support interaction destabilized the Pd^{4+} species that could maximize the reactivity of the palladium species as well.

DFT calculations were also conducted to understand the stabilities of palladium species on different rutile surface at the molecular level. Fig. 6 summarized of the DFT calculations for the binding energies of PdO and PdO_2 species on the rutile (110) and (111) surfaces. As discussed, the different arrangements of surface atoms would result in distinct steric hindrances and finally affect the existence states of the palladium species. Consequently, two configurations, the Pd_2O_2 dimer and two PdO monomers, were constructed to model the PdO species on the (110) and (111) surfaces, respectively. The results revealed that the Pd_2O_2 dimer and two PdO monomers bonded with the rutile (110) and (111) facets with comparable binding energies (−13.4 eV versus −12.5 eV), suggesting that PdO species could be stabilized by both two facets. However, the stability of the PdO_2 monomer differed significantly on the two facets, as the bond strength of the two PdO_2 monomers on (111) surface (−7.4 eV) was even weaker than that of one PdO_2 monomer on (110) surface (−8.5 eV). We have to admit that the electron transferred to the constructed PdO or PdO_2 models may be not the same as that to the palladium particles experimentally detected on our catalysts. However, the results of our DFT calculations were still in agreement with the results of our characterizations, illustrating that the strong electron donation from rutile to palladium (Fig. 4) did quench the active Pd^{4+} phase. Therefore, our results and discussions finally disclosed that the reactivity of palladium was optimal only when the facet-dependent palladium-titania interactions were at a moderate intensity.

4. Conclusion

In this work, three rutile carriers with different aspect ratios and

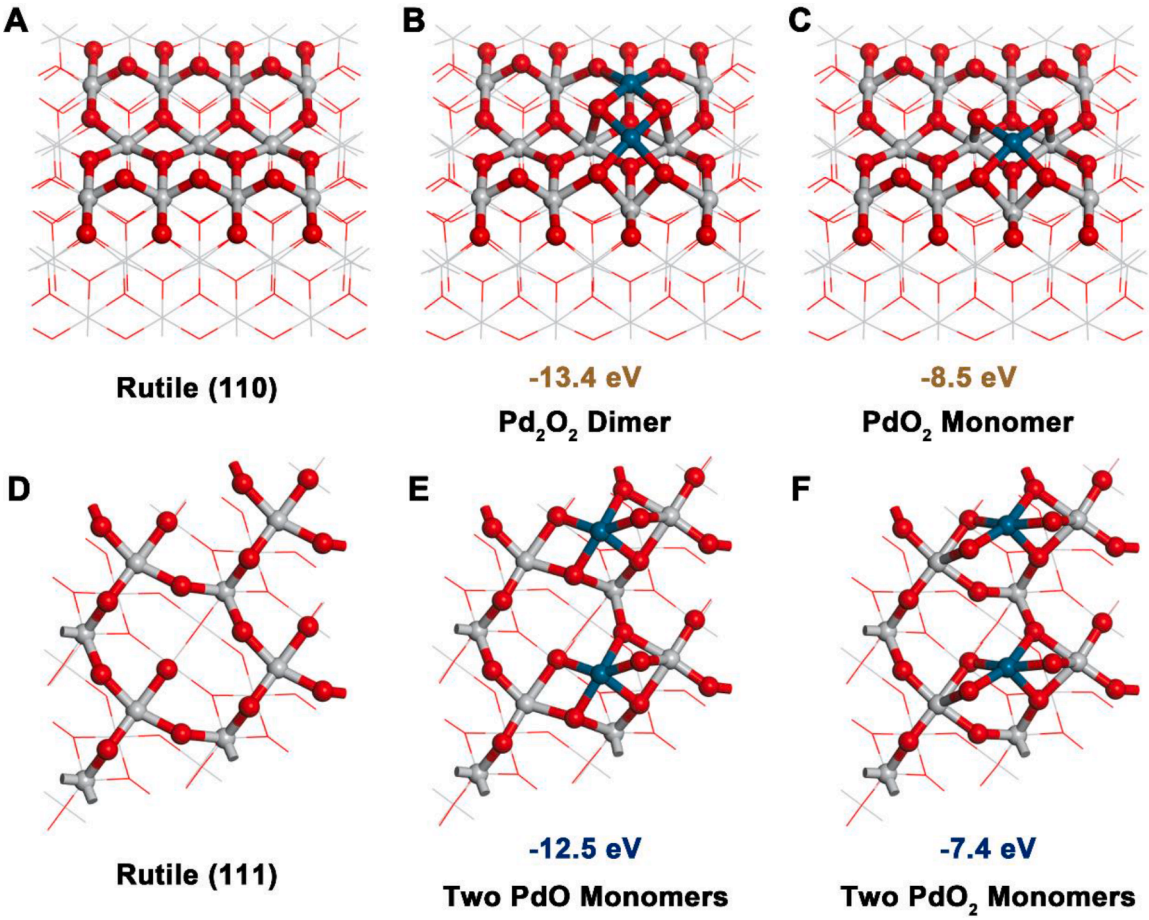

Fig. 6. The optimized configurations of the rutile (110) facet (A) before and after the deposition of (B) Pd_2O_2 dimer and (C) PdO_2 monomer. The optimized configurations of the rutile (111) facet (D) before and after the deposition of (E) two PdO monomers and (F) two PdO_2 monomers.

exposed facets were synthesized for providing an in-depth study of the facet-dependent rutile-palladium interactions. Systematic characterizations first probed the varied physiochemical properties of rutile (110) and (111) facets that originated from their different microstructures, and then revealed the effects of substrates on the particle sizes and chemical states of deposited palladium species. Detailed investigations based on palladium catalysts demonstrated that, although the stronger interaction between palladium and rutile (111) facet favored the dispersion of palladium species, it might have simultaneously induced the encapsulation of palladium by rutile. DFT calculations further elucidated that the strong electron transfer from TiO_2 (both titanium and oxygen elements) to palladium in Pd/Rutile-(111) catalyst decreased the proportion of Pd^{4+} species that could promote the activation efficiency of methane molecules. As a consequence, Pd/Rutile-(111) catalyst performed worse in CCM reaction than its Rutile-(110) supported sample instead. In other words, too strong metal-support interaction (SMSI) was actually detrimental to the reactivity of palladium for lean methane oxidation in our Pd/Rutile catalyst system.

Additional information

Competing financial interests: The authors declare no competing financial interests.

Data availability

All relevant data are available from the authors on reasonable request.

Supplementary Information is available for this paper.

CRediT authorship contribution statement

Cunshuo Li: Conceptualization, Methodology, Writing – original draft, Writing – review & editing, Methodology. **Bingyue Tang:** Methodology. **Ajibola T. Ogunbiyi:** Writing – original draft. **Songquan Tang:** Methodology. **Wenzhi Li:** Conceptualization, Methodology, Writing – review & editing, Funding acquisition. **Qiang Lu:** Methodology. **Liang Yuan:** Funding acquisition.

Declaration of Competing Interest

The authors declare that they have no known competing financial interests or personal relationships that could have appeared to influence the work reported in this paper.

Data availability

Data will be made available on request.

Acknowledgments

This work was supported by the Major Science and Technology Projects of Anhui Province (202003a05020022), the Key Research and Development Projects in Anhui Province (202004a06020053) and the Institute of Energy, Hefei Comprehensive National Science Center under Grant No. 21KZS219.

Supplementary materials

Supplementary material associated with this article can be found, in the online version, at doi:10.1016/j.mcat.2022.112475.

References

[1] W. Huang, A.C. Johnston-Peck, T. Wolter, W.C. D.Yang, L. Xu, J. Oh, et al., Steam-created grain boundaries for methane C–H activation in palladium catalysts, Science 373 (2021) 1518–1523.
[2] M. Cargnello, J.J.D. Jaén, J.C.H. Garrido, K. Bakhmutsky, T. Montini, J.J.C. Gámez, et al., Exceptional activity for methane combustion over modular $Pd@CeO_2$ subunits on functionalized Al_2O_3, Science 337 (6095) (2012) 713–717.
[3] P.S. Barbato, V. Di Sarli, G. Landi, A. Di Benedetto, High pressure methane catalytic combustion over novel partially coated $LaMnO_3$-based monoliths, Chem. Eng. J. 259 (2015) 381–390.
[4] Y. Jiang, W. Li, K. Chen, X. Zhang, C. Shen, L. Yuan, A rod-like Co_3O_4 with high efficiency and large specific surface area for lean methane catalytic oxidation, Mol. Catal. 522 (2022), 112229.
[5] R.J. Farrauto, Low-temperature oxidation of methane, Science 337 (2012) 659–660.
[6] Y. Dai, V. Pavan Kumar, C. Zhu, M.J. MacLachlan, K.J. Smith, M.O Wolf, Mesoporous silica-supported nanostructured PdO/CeO_2 catalysts for low-temperature methane oxidation, ACS Appl. Mater. Interfaces 10 (1) (2017) 477–487.
[7] E. Hong, C. Kim, D.H. Lim, H.J. Cho, C.H. Shin, Catalytic methane combustion over Pd/ZrO_2 catalysts: effects of crystalline structure and textural properties, Appl. Catal. B 232 (2018) 544–552.
[8] X. Pan, Y. Zhang, Z. Miao, X. Yang, A novel $PdNi/Al_2O_3$ catalyst prepared by galvanic deposition for low temperature methane combustion, J. Energy Chem. 22 (4) (2013) 610–616.
[9] J. Chen, Y. Wu, W. Hu, P. Qu, X. Liu, R. Yuan, et al., Insights into the role of Pt on Pd catalyst stabilized by magnesia-alumina spinel on gama-alumina for lean methane combustion: enhancement of hydrothermal stability, Mol. Catal. 496 (2020), 111185.
[10] X. Zhao, Y. Liu, J. Deng, P. Xu, J. Yang, K. Zhang, et al., Mesoporous Pd Pt alloys: high-performance catalysts for methane combustion, Mol. Catal. 442 (2017) 191–201.
[11] L. Luo, S. Wang, C. Fan, L. Yang, Z. Wu, Z. Qin, et al., Promoting effect of alkali metal cations on the catalytic performance of Pd/H-ZSM-5 in the combustion of lean methane, Appl. Catal. A 602 (2020), 117678.
[12] L. Luo, S. Wang, Z. Wu, Z. Qin, H. Zhu, W. Fan, et al., Structure and performance of supported iridium catalyst for the lean methane oxidation at low temperature, Appl. Catal. A 641 (2022), 118699.
[13] K. Murata, D. Kosuge, J. Ohyama, Y. Mahara, Y. Yamamoto, S. Arai, et al., Exploiting metal–support interactions to tune the redox properties of supported Pd catalysts for methane combustion, ACS Catal. 10 (2) (2019) 1381–1387.
[14] A.Y. Stakheev, A.M. Batkin, N.S. Teleguina, G.O. Bragina, V.I. Zaikovsky, I. P. Prosvirin, et al., Particle size effect on CH_4 oxidation over noble metals: comparison of Pt and Pd catalysts, Top. Catal. 56 (1–8) (2013) 306–310.
[15] S. Chen, S. Li, R. You, Z. Guo, F. Wang, G. Li, et al., Elucidation of active sites for CH_4 catalytic oxidation over Pd/CeO_2 via tailoring metal–support interactions, ACS Catal. 11 (9) (2021) 5666–5677.
[16] T.P. Senftle, A.C.T. van Duin, M.J. Janik, Role of site stability in methane activation on $Pd_xCe_{1-x}O_\delta$ surfaces, ACS Catal. 5 (10) (2015) 6187–6199.
[17] H. Xiong, D. Kunwar, D. Jiang, C.E. García-Vargas, H. Li, C. Du, et al., Engineering catalyst supports to stabilize PdO_x two-dimensional rafts for water-tolerant methane oxidation, Nat. Catal. 4 (10) (2021) 830–839.
[18] H. Duan, R. You, S. Xu, Z. Li, K. Qian, T. Cao, et al., Pentacoordinated Al^{3+}-stabilized active Pd structures on Al_2O_3-coated palladium catalysts for methane combustion, Angew. Chem. Int. Ed. 58 (35) (2019) 12043–12048.
[19] C. Chen, Y.H. Yeh, M. Cargnello, C.B. Murray, P. Fornasiero, R.J. Gorte, Methane oxidation on $Pd@ZrO_2/Si–Al_2O_3$ is enhanced by surface reduction of ZrO_2, ACS Catal. 4 (11) (2014) 3902–3909.
[20] K. Murata, J. Ohyama, Y. Yamamoto, S. Arai, A. Satsuma, Methane combustion over Pd/Al_2O_3 catalysts in the presence of water: effects of Pd particle size and alumina crystalline phase, ACS Catal. 10 (15) (2020) 8149–8156.
[21] W. Li, D. Liu, X. Feng, Z. Zhang, X. Jin, Y. Zhang, High-performance ultrathin Co_3O_4 nanosheet supported PdO/CeO_2 catalysts for methane combustion, Adv. Energy Mater. 9 (18) (2019), 1803583.
[22] J. Yang, M. Peng, G. Ren, H. Qi, X. Zhou, J. Xu, et al., A Hydrothermally Stable Irreducible Oxide-modified $Pd/MgAl_2O_4$ catalyst for methane combustion, Angew. Chem. Int. Ed. 59 (42) (2020) 18522–18526.
[23] A.W. Petrov, D. Ferri, F. Krumeich, M. Nachtegaal, J.A. van Bokhoven, O. Kröcher, Stable complete methane oxidation over palladium based zeolite catalysts, Nat. Commun. 9 (1) (2018).
[24] Y. Ding, Q. Wu, B. Lin, Y. Guo, Y. Guo, Y. Wang, et al., Superior catalytic activity of a Pd catalyst in methane combustion by fine-tuning the phase of ceria-zirconia support, Appl. Catal. B 266 (2020), 118631.
[25] J. Wan, W. Chen, C. Jia, L. Zheng, J. Dong, X. Zheng, et al., Defect effects on TiO_2 nanosheets: stabilizing single atomic site au and promoting catalytic properties, Adv. Mater. 30 (11) (2018), 1705369.
[26] I.X. Green, W. Tang, M. Neurock, J.T. Yates, Spectroscopic observation of dual catalytic sites during oxidation of CO on a Au/TiO_2 catalyst, Science 333 (6043) (2011) 736–739.
[27] O. Khalid, A.S. Luciano, G. Drazic, H. Over, Mixed $Ru_xIr_{1-x}O_2$ supported on rutile TiO_2 catalytic methane combustion, a model study, ChemCatChem 13 (2021) 3983–3994.
[28] X. Yuan, M. Qing, L. Meng, H. Zhao, One-step synthesis of nanostructured Cu–Mn/TiO_2 via flame spray pyrolysis: application to catalytic combustion of CO and CH_4, Energy Fuels 34 (11) (2020) 14447–14457.

[29] P. Zhang, J. Xiong, Y. Wei, Y. Li, Y. Zhang, J. Tang, et al., Exposed {0 0 1} facet of anatase TiO_2 nanocrystals in Ag/TiO_2 catalysts for boosting catalytic soot combustion: the facet-dependent activity, J. Catal. 398 (2021) 109–122.
[30] D. Mukherjee, P. Venkataswamy, D. Devaiah, A. Rangaswamy, B.M. Reddy, Crucial role of titanium dioxide support in soot oxidation catalysis of manganese doped ceria, Catal. Sci. Technol. 7 (14) (2017) 3045–3055.
[31] M. Tang, S. Li, S. Chen, Y. Ou, M. Hiroaki, W. Yuan, et al., Facet-dependent oxidative strong metal-support interactions of palladium–TiO_2 determined by *in situ* transmission electron microscopy, Angew. Chem. Int. Ed. 60 (41) (2021) 22339–22344.
[32] F. Bertella, P. Concepción, A. Martínez, TiO_2 polymorph dependent SMSI effect in Co-Ru/TiO_2 catalysts and its relevance to Fischer-Tropsch synthesis, Catal. Today 289 (2017) 181–191.
[33] L. Yu, K. Sato, T. Toriyama, T. Yamamoto, S. Matsumura, K. Nagaoka, Influence of the crystal structure of titanium oxide on the catalytic activity of Rh/TiO_2 in steam reforming of propane at low temperature, Chem. Eur. J. 24 (35) (2018) 8742–8746.
[34] D.A.H. Hanaor, C.C. Sorrell, Review of the anatase to rutile phase transformation, J. Mater. Sci. 46 (4) (2010) 855–874.
[35] Y. Xiao, J. Li, C. Wang, F. Zhong, Y. Zheng, L. Jiang, Construction and evolution of active palladium species on phase-regulated reducible TiO_2 for methane combustion, Catal. Sci. Technol. 11 (3) (2021) 836–845.
[36] Z. Rui, Y. Huang, Y. Zheng, H. Ji, X. Yu, Effect of titania polymorph on the properties of CuO/TiO_2 catalysts for trace methane combustion, J. Mol. Catal. A Chem. 372 (2013) 128–136.
[37] Z. Hu, X. Liu, D. Meng, Y. Guo, Y. Guo, G. Lu, Effect of ceria crystal plane on the physicochemical and catalytic properties of Pd/ceria for CO and propane oxidation, ACS Catal. 6 (4) (2016) 2265–2279.
[38] Y. Lei, W. Li, Q. Liu, Q. Lin, X. Zheng, Q. Huang, et al., Typical crystal face effects of different morphology ceria on the activity of Pd/CeO_2 catalysts for lean methane combustion, Fuel 233 (2018) 10–20.
[39] K. Chen, W. Li, Z. Zhou, Q. Huang, Y. Liu, Q. Duan, Hydroxyl groups attached to Co^{2+} on the surface of Co_3O_4: a promising structure for propane catalytic oxidation, Catal. Sci. Technol. 10 (8) (2020) 2573–2582.
[40] Y. Jian, M. Tian, C. He, J. Xiong, Z. Jiang, H. Jin, et al., Efficient propane low-temperature destruction by Co_3O_4 crystal facets engineering: unveiling the decisive role of lattice and oxygen defects and surface acid-base pairs, Appl. Catal. B 283 (2021), 119657.
[41] M. Chen, J. Ma, B. Zhang, F. Wang, Y. Li, C. Zhang, et al., Facet-dependent performance of anatase TiO_2 for photocatalytic oxidation of gaseous ammonia, Appl. Catal. B 223 (2018) 209–215.
[42] B. Fu, Z. Wu, K. Guo, L. Piao, Rutile TiO_2 single crystals delivering enhanced photocatalytic oxygen evolution performance, Nanoscale 13 (18) (2021) 8591–8599.
[43] Y. Yamazaki, M. Fujitsuka, S. Yamazaki, Effect of organic additives during hydrothermal syntheses of rutile TiO_2 nanorods for photocatalytic applications, ACS Appl. Nano Mater. 2 (9) (2019) 5890–5899.
[44] A. Mamakhel, C. Tyrsted, E.D. Bøjesen, P. Hald, B.B. Iversen, Direct formation of crystalline phase pure rutile TiO_2 nanostructures by a facile hydrothermal method, Cryst. Growth Des. 13 (11) (2013) 4730–4734.
[45] L. Yu, K. Sato, T. Toriyama, T. Yamamoto, S. Matsumura, K. Nagaoka, Influence of the crystal structure of titanium oxide on the catalytic activity of Rh/TiO_2 in steam reforming of propane at low temperature, Chemistry 24 (35) (2018) 8742–8746.
[46] Z. Yang, B. Wang, J. Zhang, H. Cui, Y. Pan, H. An, et al., Factors influencing the photocatalytic activity of rutile TiO_2 nanorods with different aspect ratios for dye degradation and Cr(VI) photoreduction, Phys. Chem. Chem. Phys. 17 (28) (2015) 18670–18676.
[47] T. Tatarchuk, N. Danyliuk, A. Shyichuk, W. Macyk, M. Naushad, Photocatalytic degradation of dyes using rutile TiO_2 synthesized by reverse micelle and low temperature methods: real-time monitoring of the degradation kinetics, J. Mol. Liq. 342 (2021), 117407.
[48] L. Lin, Z. Shi, J. Huang, P. Wang, W. Yu, C. He, et al., Molecular adsorption properties of CH_4 with noble metals doped onto oxygen vacancy defect of anatase TiO_2 (1 0 1) surface: first-principles calculations, Appl. Surf. Sci. 514 (2020), 145900.
[49] J. Wang, M. Lei, Z. Wang, Y. Liu, W. Zhuang, W. Zhu, Methanol oxidation over rutile Au_1@TiO_2 catalyst: importance of facets and oxygen vacancy, Appl. Surf. Sci. 542 (2021), 148541.
[50] Z. Ren, Z. Wu, W. Song, W. Xiao, Y. Guo, J. Ding, et al., Low temperature propane oxidation over Co_3O_4 based nano-array catalysts: ni dopant effect, reaction mechanism and structural stability, Appl. Catal. B 180 (2016) 150–160.
[51] W. Tang, J. Weng, X. Lu, L. Wen, A. Suburamanian, C.Y. Nam, et al., Alkali-metal poisoning effect of total CO and propane oxidation over Co_3O_4 nanocatalysts, Appl. Catal. B 256 (2019), 117859.
[52] Z. Rui, S. Wu, C. Peng, H. Ji, Comparison of TiO_2 Degussa P25 with anatase and rutile crystalline phases for methane combustion, Chem. Eng. J. 243 (2014) 254–264.
[53] Y. Wang, H. Arandiyan, J. Scott, M. Akia, H. Dai, J. Deng, et al., High performance Au–Pd supported on 3D hybrid strontium-substituted lanthanum manganite perovskite catalyst for methane combustion, ACS Catal. 6 (10) (2016) 6935–6947.
[54] C. Li, W. Li, K. Chen, A.T. Ogunbiyi, Z. Zhou, F. Xue, et al., Palladium nanoparticles supported on surface-modified metal oxides for catalytic oxidation of lean methane, ACS Appl. Nano Mater. 3 (12) (2020) 12130–12138.
[55] W. Barrett, J. Shen, Y. Hu, R.E. Hayes, R.W.J. Scott, N. Semagina, Understanding the role of SnO_2 support in water-tolerant methane combustion: *in situ* observation of $Pd(OH)_2$ and comparison with Pd/Al_2O_3, ChemCatChem 12 (3) (2019) 944–952.
[56] Y. Zhang, J. Zhu, S. Li, Y. Xiao, Y. Zhan, X. Wang, et al., Rational design of highly H_2O- and CO_2-tolerant hydroxyapatite-supported Pd catalyst for low-temperature methane combustion, Chem. Eng. J. 396 (2020), 125225.
[57] C. Li, W. Li, K. Chen, A.T. Ogunbiyi, Z. Zhou, Q. Duan, et al., Highly active Pd catalysts supported on surface-modified cobalt-nickel mixed oxides for low temperature oxidation of lean methane, Fuel 279 (2020), 118372.
[58] T.P. Senftle, A.C.T. van Duin, M.J. Janik, Methane activation at the Pd/CeO_2 interface, ACS Catal. 7 (1) (2016) 327–332.